A novel aerosol filter sampler for measuring the vertical distribution of ice-nucleating particles via fixed-wing uncrewed aerial vehicles

Alexander Böhmländer[1], Larissa Lacher[1], David Brus[2], Konstantinos-Matthaios Doulgeris[2], Zoé Brasseur[3], Matthew Boyer[3], Joel Kuula[2], Thomas Leisner[1], and Ottmar Möhler[1]

[1]Institute of Meteorology and Climate Research, Karlsruhe Institute of Technology, Karlsruhe, Germany
[2]Atmospheric Composition Research, Finnish Meteorological Institute, Helsinki, Finland
[3]Institute for Atmospheric and Earth System Research/Physics, Faculty of Science, University of Helsinki, Helsinki, Finland
Correspondence: Ottmar Möhler (ottmar.moehler@kit.edu)

Abstract. A mobile sampler for collecting aerosol particles on an uncrewed aerial vehicle (UAV) was developed and tested during three consecutive Pallas Cloud Experiment campaigns in the vicinity of the Sammaltunturi Global Atmosphere Watch site (67°58' N, 24°7' E, 565 m above sea level) in Finland. The sampler is designed to collect aerosol particles onto Nuclepore filters, which are subsequently analysed for the temperature-dependent number concentration of ice-nucleating particles of the sampled aerosol using a freezing assay. The sampler was flown with a fixed-wing UAV in different altitudes up to 1000 m above ground level. The total flight time ranges from 60 min to around 100 min, depending on environmental conditions. Pressure, temperature and relative humidity are also measured to provide information about the meteorological flight conditions. The flow over the filter was maintained by a micro-diaphragm pump, providing around 10 standard litres per minute over a small filter (diameter of 25 mm) and around 11 standard litres per minute over a larger filter (diameter of 47 mm) at a pressure corresponding to 500 m above sea level. For a typical flight time of 1.5 hours, this results in a sampled air volume of about 930 to 1000 standard litres per flight, giving an INP detection limit of approximately 1.1×10^{-3} and 1.0×10^{-3} INPs per standard litre, respectively. For comparison to the flight results, a similar setup was deployed at ground level. The comparison shows a clear distinction from the water and handling blank background for both setups, proving the technical feasibility of the setups. Furthermore, for some flights, a shift between the two INP populations can be seen, indicating that ground-based INP measurements deviate from the samples collected on-board the UAV.

1 Introduction

Ice-nucleating particles (INPs) are a rare subset of aerosol particles, which induce primary ice formation inside clouds, and therefore play special and important roles in aerosol-cloud interactions. The formulation and quantification of these interactions are largely uncertain in current weather and climate models (Boucher et al., 2013; IPCC, 2021; Murray et al., 2021). While cloud water droplets can freeze homogeneously only below about -35 °C (e.g., Pruppacher and Klett, 1997), INPs decrease the threshold for ice nucleation, and therefore enable water droplets to freeze well above -35 °C (e.g., Vali, 1996; Pruppacher and Klett, 1997; Murray et al., 2012; Hoose and Möhler, 2012; Kanji et al., 2017). In this way, INPs significantly contribute to primary ice formation, which impacts the depletion of supercooled water inside mixed-phase clouds (e.g., Wegener, 1911;

Bergeron, 1935; Findeisen, 1938; Shi and Liu, 2019). The ratio of ice crystals and supercooled water droplets also largely impacts the cloud albedo and therefore the radiation budget of Earth (e.g., Korolev et al., 2017; Lohmann, 2017; Storelvmo, 2017; Desai et al., 2019; Shi and Liu, 2019). Furthermore, about $50\,\%$ of all precipitation events of more than $1\,mm$ per day are linked to the occurrence of the ice phase in the cloud, and this value increases to more than $90\,\%$ for polar regions (Field and Heymsfield, 2015; Mülmenstädt et al., 2015; Heymsfield et al., 2020). Most field observations measure INPs at ground- or aircraft-level (e.g., DeMott et al., 2010, 2017; Kanji et al., 2017; Schneider et al., 2021; He et al., 2021), and it is not yet sufficiently understood how to connect ground-based INP measurements with cloud formation processes. While aircraft can be used to measure INP concentrations at the level of cloud formation, these measurements are not feasible for longer-term studies due to the high operational costs.

Recently, uncrewed aerial vehicles (UAVs) have become one of the focuses for atmospheric measurements (e.g., Bärfuss et al., 2018; Lampert et al., 2020; Marinou et al., 2019; Villa et al., 2016; Yu et al., 2017). Some studies have been performed to measure INPs on a UAV (Schrod et al., 2017; Bieber et al., 2020) or with balloon-based sampling systems (Creamean et al., 2018; Porter et al., 2020). Bieber et al. (2020) used a multicopter to measure biogenic INPs up to $100\,m$ above ground level (agl) with flight times of 10 minutes. Longer sampling times (< 90 minutes) and higher altitudes (< $2.5\,km$ agl) were reached with a setup using two fixed-wing UAVs (Schrod et al., 2017), enabling measurements of the vertical INP distribution during dust events in the Eastern Mediterranean. Creamean et al. (2018) developed a lightweight system to measure the INP concentration of aerosol particles deposited on a filter via a launched balloon. The system was tested up to an altitude of $1.1\,km$ agl and also measures the total particle concentration. A balloon-based size-resolved INP sampler was developed by Porter et al. (2020) and was deployed during campaigns in Hyytiälä (southern Finland), Leeds (northern England), Longyearbyen (Svalbard, Norway), and Cardington (southern England). The payload is tethered at a specific height (< $2.3\,km$) with a winch and can sample up to 11 hours. In general, the sampling time as well as the sample flow over a filter determine the lower detection limit for INPs. This lower detection limit is especially relevant at higher subzero temperatures, where the INP concentration is orders of magnitudes lower than at lower temperatures (e.g., DeMott et al., 2010; Kanji et al., 2017).

In this study, we present a filter-based aerosol sampler flown on a fixed-wing UAV. A fixed-wing UAV is able to provide longer flight durations as well as a constant airspeed compared to multicopter UAVs. The main advantage of a UAV is the flexibility of use as well as the low operational costs compared to an aircraft or balloon-borne setup. No runway is needed, and the fixed-wing can be started and deployed by two people in a matter of minutes, only hindered by flight regulations and weather restrictions.

2 Experimental

2.1 Flight platform

The UAV used to carry the payload is a Skywalker 1830 model year 2015 (customised by Yugen Oy). The Skywalker is a fixed-wing UAV with a wingspan of $1830\,mm$ and a maximum takeoff mass of $3000\,g$. The maximum payload weight of the Skywalker is approximately $1200\,g$. The fuselage is $220\,mm$ long with a width of $120\,mm$ and can be accessed via two

Figure 1. The Skywalker shown with the final setup after a successful flight. The filter holder is installed with a tube connection through the wooden side plate. The inlet is blocked until launch. On the right, the ambient sensor (BME280, Bosch) can be seen, and the airspeed sensor is visible on the left side (ASPD-7002, Matek Systems).

openings covered with wooden plates (150 mm x 75 mm) on both sides. The Skywalker is powered by two LiIon batteries (4S, 7000 mA h) connected in parallel, providing a maximum flight time of about 2 hours in ideal weather conditions. It is a glider-type airframe, enabling long flight duration at one altitude at low power consumption. It can be launched by hand and

60 just needs a flat surface (i.e. grass) for landing on the belly. These features make the Skywalker a well-suited UAV for filter-based aerosol sampling. The Skywalker contains additional components, such as a flight controller using arduplane firmware 4.06 (F405-WING, Matek Systems), an analogue airspeed sensor (ASPD-7002, Matek Systems) and a compass module (M8Q-4883, Matek Systems). The data from the compass module is used to track the UAV flight path via global navigation satellite system (GNSS) data.

65 **2.2 Payload**

The aerosol sampling setup developed here was tested and improved during three field campaigns in Pallas, Finland. During the first campaign in autumn 2020, the whole payload was located inside the fuselage and the aerosol inlet was located below the left wing, resulting in a sampling line with two 90° bends. This setup proved the technical feasibility of measuring INPs with sample times between 45 and 90 minutes in regions with low aerosol concentrations, such as the area around Sammaltunturi in

70 northern Finland during the measurement periods in spring and autumn. While low aerosol concentrations might also lead to

Table 1. UAV-based aerosol sampler. Description of the used components in the UAV-based aerosol sampler. The total weight of the sampling unit is about 870 g. Sensor specifications are from the respective data sheets (Sensirion, 2013; Bosch, 2020; Sensirion, 2021).

Name	Description	Details
Inlet[a]	Inner diameter: 6 mm	stainless steel, antistatic tubing
	Length: 17.2 cm (14.2 cm[b])	
Filter holder	Diameter: 25 (47[c]) mm	polypropylene, Whatman, 420200 (420400[c])
	Weight: 10 (62[c]) g	
Filter	Diameter: 25 (47[c]) mm	Nuclepore, Whatman, 110637 (111137[c])
	Pore size: 0.4 μm	
Flow meter	Pressure drop: < 25 hPa	Sensirion SFM4100 Air
	Flow range: $0–20\,\mathrm{l_{std}\,min^{-1}}$	
	Accuracy: 0.15 % of full scale or 3 % of reading, whichever is bigger	
Pump	Weight: 380 g	KNF, NMP850.1.2KPDC-B HP
	Flow at 1013 hPa: $15\,\mathrm{l\,min^{-1}}$	
	$I_{\max} = 2.4\,\mathrm{A}, U = 12\,\mathrm{V}$	
Single board computer	Weight: 9 g	Raspberry Pi Zero WH
LiIon battery	Weight: 280 g	4S
	Capacity: 3300 mA h	
Ambient sensor 1	T: -40–85 °C	Bosch Sensortec BME280
	RH: 0–100 %RH	
	p: 300–1100 hPa	
Ambient sensor 2	T: -40–125 °C	Sensirion SHT40
	RH: 0–100 %RH	

[a] The third version of the setup does not use an inlet.

[b] The second version has a decreased length of the inlet.

[c] The third version of the setup contains the larger filter holder.

lower INP concentrations, this is not always true, since some aerosols might be much more ice active than others and therefore contribute disproportionally to the INP concentration (e.g., Hoose and Möhler, 2012). For the second version deployed in spring 2021, the filter holder was placed below the batteries in the front of the UAV, with a short straight horizontal tube as the aerosol inlet upstream of the filter. This change enhanced the theoretical sampling efficiency of larger aerosol particles due to fewer bends (see app. B for an estimation of the transport efficiency for the different setups). For the third setup used during autumn 2021, the filter holder was placed outside of the fuselage, below the wing (setup depicted in Fig. 1). In the following, this third and final setup is described in more detail (see also Table 1). In each setup, the payload contains a micro-diaphragm pump (NMP850.1.2KPDC-B HP, KNF), which provides a flow of $15\,\mathrm{l\,min^{-1}}$ at standard conditions (KNF). The pump weighs

Figure 2. 3D printed parts for the filter holder mounting to the plane. From left to right: mount base, mount backplate, filter holder mount and final setup. The mount base is connected to the wing by the backplate, while the filter holder snaps into the base and secures the position of the filter holder.

$380\,\mathrm{g}$ and draws a maximum current of $2.4\,\mathrm{A}$ at a voltage of $12\,\mathrm{V}$. The pump is connected to a mass flow meter (SFM4100,
Sensirion) to monitor the flow during the sampling, which depends on the ambient pressure conditions, and therefore varies at different sampling altitudes. The mass flow meter is read out with a single board computer (SBC; Raspberry Pi Zero WH, Raspberry Pi) at a frequency of $1\,\mathrm{Hz}$, and is used to identify issues during the operation, i.e. connection failures or clocking of the filter pores. Upstream of the flow meter, a plastic filter holder (420400, Whatman) with a diameter of $47\,\mathrm{mm}$ and a weight of roughly $62\,\mathrm{g}$ is connected and mounted below the right wing (see Fig. 1). The mount is a 3D printed piece that can be quickly connected and disconnected to the wing (see Fig. 2). The whole payload is powered by a LiIon battery ($3300\,\mathrm{mA\,h}$) for more than 2 hours. In addition, the SBC is also used to read out two sensors at the front of the UAV (BME280, Bosch Sensortec, and SHT40, Sensirion), providing temperature T, pressure p, and relative humidity RH data with an uncertainty of $\pm\,1.0\,\mathrm{K}$ ($0.2\,\mathrm{K}$ for SHT40), $\pm\,1.0\,\mathrm{hPa}$ (only BME280) and $\pm\,3\,\%\mathrm{RH}$ ($1.8\,\%\mathrm{RH}$ for SHT40), respectively (Bosch, 2020; Sensirion, 2021). The pressure data of the BME280 is used to calculate the flow during the flight (see app. C). All components are detailed in Table 1, and a schematic view is presented in Figure 3. A second identical ground-based sampling system consists of the same components as the UAV sampler.

2.3 Typical flight operation

Prior to each flight, the filter holder is loaded with a Nuclepore filter (111137, Whatman). While the filter holder is installed, the inlet of the sample tube is closed with a cap, which is removed right before the start of the flight. During the preparations for each flight, the autopilot mission is uploaded onto the flight controller using MissionPlanner (version 1.3.74), the SBC is connected to the batteries, and the respective scripts are started to read out the flow meter and the meteorological sensors. After the UAV is hand-launched, it is flown manually to the designated altitude. Once the UAV reaches the targeted altitude, the autopilot is turned on to initiate a loiter command that steers the UAV in circles with $200\,\mathrm{m}$ radius above the measurement
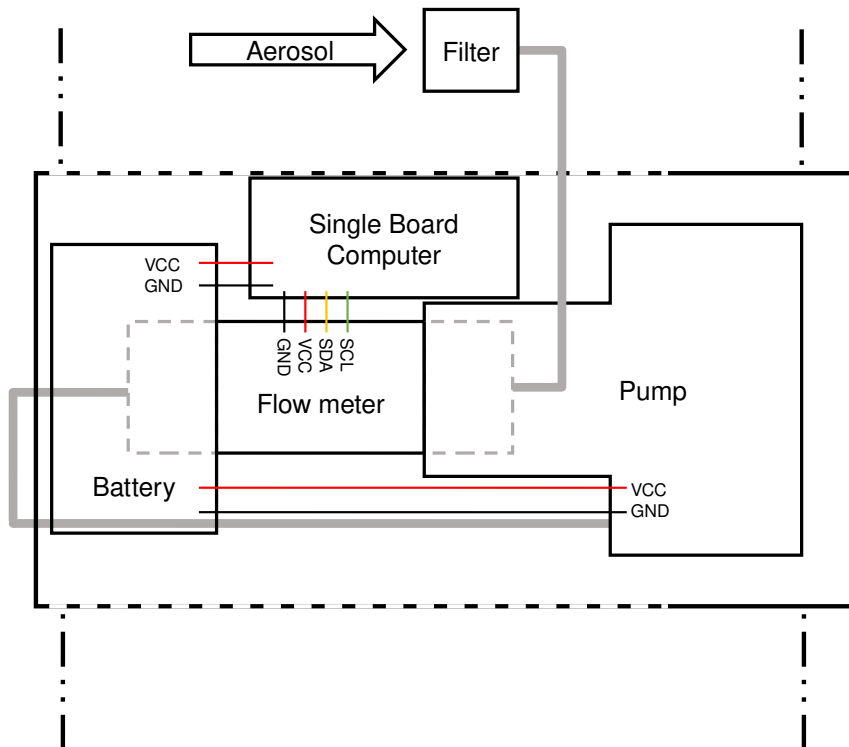
Figure 3. Schematic view from the top of the setup. The fuselage is shown with the wings in the bottom and top marked by the vertical dash-dotted lines. The cover plates are indicated by the dashed horizontal lines. The pump connections are shown for the filter in grey with an arrow to indicate the flow of the aerosol. The electrical connections are drawn for the power (VCC, voltage at the common collector; GND, ground) as well as for the data connection via I2C for the flow meter (SCL, serial clock; SDA, serial data). For simplicity, the data connections to the two ambient sensors SHT40 and BME280, which are also read by the single-board computer via I2C, are not shown.

field, keeping the same altitude during the remainder of the flight (see Fig. 4). At the same time, the pump is turned on remotely via radio switch to start sampling aerosol particles, making sure that aerosol particles are only actively sampled at one altitude. The start-up procedure, including the ascend time, typically takes less than 10 minutes, depending on the targeted sampling altitude. Once the pump of the UAV sampler is turned on, the ground-based aerosol sampling (location shown in Fig. 4, red cross) is started as well, providing a temporal overlap of the collection times for comparing the INP concentrations measured at ground level and UAV flight altitude. Figure 5 shows a typical timeseries of the sensor data during one flight experiment. The SHT40 has a lower uncertainty compared to the BME280 but only measures the temperature and the relative humidity. The pressure data is important for the setup since it is used to calculate the sampling flow.
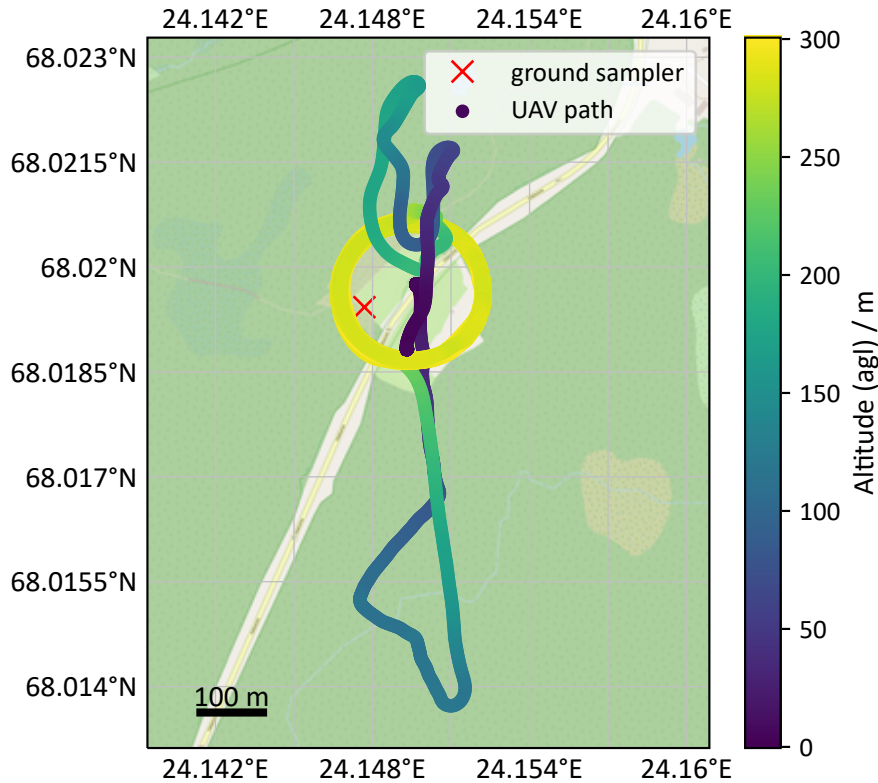
Figure 4. Typical flight path of the Skywalker during an experiment at 300 m agl at the sampling location in Pallas, Finland. The colour indicates the altitude agl as given by the GNSS measurements from the flight controller, while a red cross marks the position of the ground sampler on top of a wooden hut (about 2 m agl). Map data from $^{©}$OpenStreetMap. Distributed under the Open Data Commons Open Database License (ODbL) v1.0.

2.4 Filter handling and subsequent offline INP analysis

The Nuclepore filters used for aerosol collection are pre-cleaned with 10% H_2O_2 and afterwards rinsed with Nanopure water (generated by Barnstead GenPure Pro UV), which was passed through a 0.1 µm syringe filter (6784-2501, Whatman). The clean filters are then dried on aluminium foil under a constant clean air flow and afterwards packaged in pairs inside pre-heated aluminium foil. During handling of the filters, forceps that are pre-cleaned the same way and packaged in aluminium foil are used. After aerosol collection on the UAV or with the ground-based setup, the filters are stored in sterile Petri dishes, packed inside aluminium foil, and stored until analysed by the Ice Nucleation Spectrometer of the Karlsruhe Institute of Technology (INSEKT, see e.g., Schneider et al., 2021). The results shown in this paper are obtained from filters stored for around 45 days at -20 °C before analysis. The INP background from the sampling method is quantified by taking handling blanks that show possible contaminations during handling. The handling blanks are loaded onto the filter holder; the filter holder is mounted
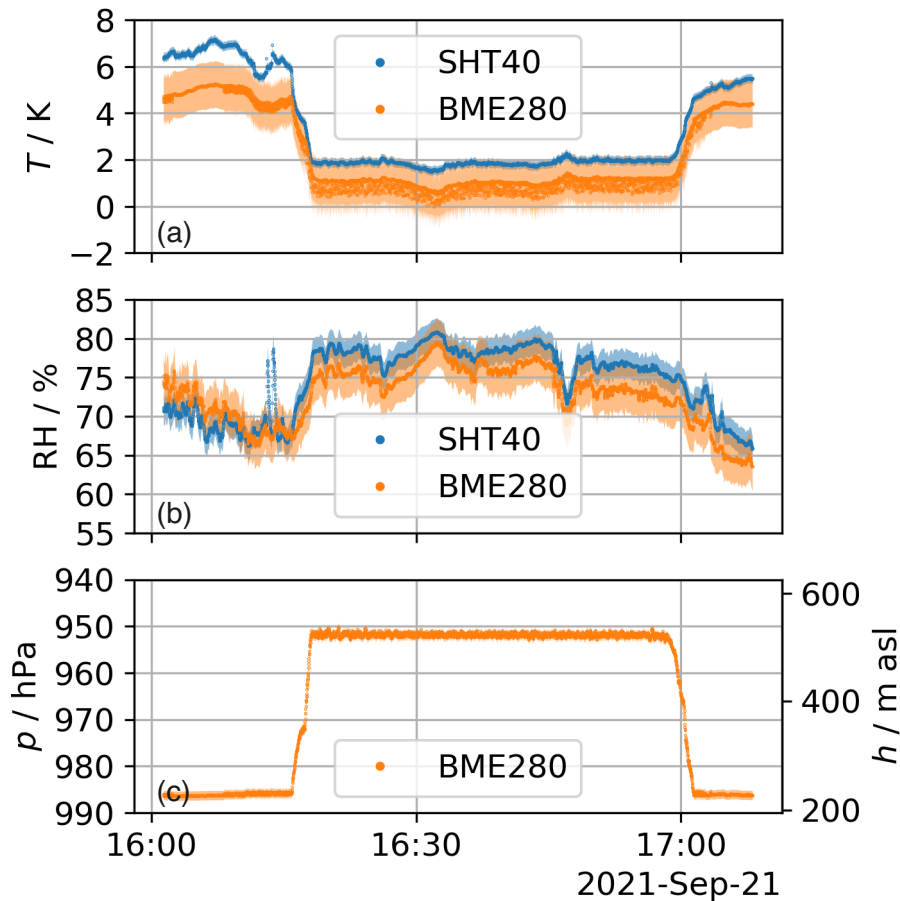
Figure 5. Typical sensor data during an experiment at 300 m agl. The three parameters temperature T, relative humidity RH and pressure p are shown for the two sensors (blue line, SHT40, orange dotted, BME280) in panels (a), (b) and (c), respectively. In addition, the height is calculated with the barometric height formula and plotted on the right y axis in panel (c), depicting the ascend and descend, as well as the loitering above the ground. The uncertainty bands for both sensors show that the measurements are in agreement. Only the temperature shows a statistically significant difference before and after the flight. This might be due to the fact that the sensors are located on different sides of the UAV, influenced by sun radiation. This difference is decreasing during loitering, where both sensors will be facing the sun at different times during the flight.

on the UAV, but the pump is not turned on; afterwards, the handling blanks are compared to the sampled filters to make sure that the collected aerosol stems from the measurement and not from contaminations during the handling. For a more detailed description of potential contaminations and procedures during filter handling, see e.g., Barry et al. (2021).

120   Before analysis with INSEKT, collected aerosol particles are washed off the filter inside centrifuge tubes with 5–8 ml Nanopure water generated by Barnstead GenPure Pro UV and filtered through an additional 0.1 µm syringe filter (6784-2501, What-

man). After tumbling at 60 rpm (1 Hz) for 20 minutes, the washing water is filled into 64 PCR wells, while 32 PCR wells are filled with the filtered Nanopure water.

INSEKT consists of two aluminium incubation blocks for holding 96-well polymerase chain reaction (PCR) plates (Cat. No. 781368, Brand). The blocks are temperature controlled by a cooling liquid from a cryostat (Proline RP855 for INSEKT1, Pro RP 245 E for INSEKT2, Lauda). The whole setup is enclosed inside a polyvinyl chloride (PVC) box, which is insulated by 2 cm thick ArmaFlex insulation material. The PVC box is topped by a removable anti-reflection coated glass pane. The glass pane protects the samples from contamination with ambient aerosol particles during the analysis. To prevent condensation on the glass pane, a flow of cooled, dry, synthetic air passes over it. Eight Pt100 temperature sensors (PT100 A 20/050 (NB), class A, Electronic Sensor GmbH) are placed inside evenly spaced drilled holes inside the aluminium blocks, and their data is read out with a custom-made LabVIEW programme. The Pt100 sensors are additionally calibrated, resulting in a systematic standard deviation of about 0.02 K, while the statistical standard deviation is about one order of magnitude higher. A camera is located above the freezing array, filming the PCR plates through a polarisation filter. The freezing array is cooled down at a rate of 0.33 K min^{-1}. The freezing of a well results in an abrupt change in its recorded grayscale value. From the amount of frozen wells in comparison to the total amount of wells, the liquid fraction, f_l, can be calculated, and from that the INP concentration in the solution, $c_\mathrm{INP}^\mathrm{sol}$, according to

$$c_\mathrm{INP}^\mathrm{sol} = -\frac{d}{V_\mathrm{well}} \ln(f_\mathrm{l}) \, , \tag{1}$$

where d is the dilution scale and V_well the volume of one PCR well (50 µl). The water background, which is obtained by adding pure Nanopure water to some wells, gets subtracted from the INP concentration in the solution according to its liquid fraction.

Combined with the mass flow over the filter, F_std, and the sampling time, t_sample, the INP concentration in standard litres of air, $c_\mathrm{INP}^\mathrm{air}$, can be calculated via

$$c_\mathrm{INP}^\mathrm{air} = \frac{V_\mathrm{sol}}{F_\mathrm{std} t_\mathrm{sample}} c_\mathrm{INP}^\mathrm{sol} \, . \tag{2}$$

For a more detailed look into INSEKT and the used formulas, see Hill et al. (2016); Schneider et al. (2021); Vali (1971); Creamean et al. (2024).

2.5 Uncertainty and lower detection limit

The measured INP concentration per standard litre of air has a statistical uncertainty, described by the Wilson interval (Agresti and Coull, 1998). The systematic uncertainty is calculated from the uncertainties of the aerosol sample measurements and the water volumes filled into the PCR wells for the INSEKT analysis, the latter of which results from the pipettes used to fill the PCR wells (Schneider et al., 2021). The systematic uncertainty is roughly two orders of magnitude smaller than the statistical uncertainty, therefore it is not shown in the plots (see app. A for the detailed uncertainty calculation).

The lower detection limit can be estimated by the condition that a single INP has to exist to initiate freezing, i.e. for a sampled volume of $V = 500 \, \mathrm{l_{std}}$, the rough estimate for the lower detection limit for the INP concentration is $c_\mathrm{INP,low}^* = V^{-1} = 2 \cdot 10^{-3} \, \mathrm{l_{std}}^{-1}$. This rough detection limit however, does not factor in that only a fraction of the whole suspension is

used for one analysis. When accounting for the analysed water fraction, an improved estimate of the lower detection limit is given by the product of the analysed water fraction and the earlier estimate

$$c_{\mathrm{INP,low}} = c_{\mathrm{INP,low}}^* \frac{V_{\mathrm{sol}}}{V_{\mathrm{well}} n_{\mathrm{filled}}} \ , \tag{3}$$

where n_{filled} is the number of wells filled with the suspension. For a typical solution volume of $5\,\mathrm{ml}$ and 64 wells used for the analysis, the improved estimate is around 1.5 higher than the rough estimate. The lower detection limit is especially important for higher nucleation temperatures, where INPs are generally more rare (e.g., Kanji et al., 2017).

3   First application in field campaigns

The newly developed UAV-based aerosol sampler was used and further developed during three Pallas Cloud Experiment campaigns, close to the Sammaltunturi Global Atmosphere Watch (GAW) site (67°58'N 24°7'E, $565\,\mathrm{m}$ above sea level (asl), northern Finland, Lohila et al., 2015), which took place during autumn 2020, spring 2021, and autumn 2021. The measurement site is located in a clean subarctic environment around $180\,\mathrm{km}$ north of the Arctic circle. Snow is abundant between November and May, and low-level clouds have a typical occurrence of around $40\,\%$ during autumn (Hatakka et al., 2003).

A summary of the campaigns is shown in Table 2. A total of 28 flights have been conducted at heights ranging from $100\,\mathrm{m}$ agl to $1000\,\mathrm{m}$ agl. The flights were conducted at the Finnish Meteorological Institute (FMI) Arctic UAV base, located within a temporary danger area (TEMPO-D Pallas), 7 x $7\,\mathrm{km}$ with a ceiling of $2000\,\mathrm{m}$ agl and centred around the Sammaltunturi GAW site. This danger area allows the use of uncrewed aircraft beyond visual line of sight. Campaign 1, during autumn 2020, was used to test the first version of the setup in the field (see Sect. 3.1). A second improved version of the setup was tested in campaign 2 during spring 2021 and is described in section 3.1. The final setup was tested between 20th and 23rd September 2021 (see Sect. 3.2).

3.1   Campaign 1 & Campaign 2

Campaign 1 demonstrated the technical feasibility of the new UAV aerosol sampler in combination with the INSEKT INP analysis. The frozen fraction of a UAV and a corresponding ground filter from campaign 1 is shown in Fig. 6. The frozen fraction of the undiluted sample shows a clear separation from the water background. To demonstrate the scientific feasibility, the frozen fraction of the UAV and ground filters are compared to their respective handling blank filters taken during campaign 2, when one handling blank filter was taken for the UAV and one for the ground. For campaign 2, the setup was modified slightly (see Sect. 2.2), and in addition, the same filter was used for sampling during two consecutive flights. The flow over the filter is calculated by the mean pressures during sampling. The actual flow is the weighted arithmetic mean, where the weight is defined by the sampling time for each flight. Figure 7 shows the frozen fraction as a function of the freezing temperature for all UAV filters, one blank filter, and its respective water background on panel (a). Panel (b) shows the same for the ground-based filters. The UAV filter suspensions contain aerosols sampled between 250 and $1000\,\mathrm{m}$ agl, whereas the blank filter was handled as described in subsection 2.4. While the blank filter suspension is close to the water background, the UAV filter suspensions

Table 2. Description of the campaigns. During the first campaign, the first setup was used, while the second campaign already featured the improved setup with a straight inlet coming from the front of the UAV. The last campaign features the newest developments with a filter holder connected directly to a wing.

	Number of flights	Min / max height agl	Start	End	Setup change
Campaign 1	13	100 m / 800 m	2020-09-22	2020-09-30	proof of concept of the setup
Campaign 2	12	250 m / 1000 m	2021-04-19	2021-04-22	removal of bends in the sampling line leads to a decrease in sampling losses
Campaign 3	03	150 m / 300 m	2021-09-20	2021-09-23	shorter sampling line decreases diffusional losses, filter with a bigger diameter provides a lower pressure drop, leading to an increase in flow

show a clear separation from the water background and the handling blank background for temperatures below 253 K. The frozen fraction of the UAV filter suspension starts to freeze at temperatures about 2–7 K higher than the handling blank and the water background, showing that enough INPs were collected during the flight to enable detection. The handling blank suspension shows a slight deviation from its water background at higher temperatures (> 253 K), but is still below the level of the UAV filter suspensions, demonstrating that the handling in the field does not significantly contribute to a contamination of INPs.

The ground filter suspensions show a spread over 7 K, showing a clear separation from the handling blank suspension as well as the water background. The resulting INP concentration is shown as a function of the freezing temperature in Fig. 8 (panel (b), 500 m agl) in comparison to a one-flight filter measured one day before (panel (a), 400 m). By effectively doubling the flight time, more air is sampled, which in turn lowers the limit of detection, which is marked with a red horizontal line. Furthermore, the two samples show two different vertical distributions for the INP concentration. While panel (a) shows a very good agreement between ground and UAV filter suspension, panel (b), which was flown one day afterwards 100 m higher, shows a difference between the two filters, especially at temperatures above 256 K. This difference, albeit small, highlights the importance of measuring the vertical distribution of INPs to evaluate their influence on cloud microphysics. The data presented in this study demonstrate that such investigation is possible with the UAV sampling system described herein.

3.2 Campaign 3

The modified sampler design used during campaign 3 was significantly easier to use in the field compared to the two prior setups and also offered a higher flow due to the switch from a 25 mm diameter filter to the 47 mm diameter filter, which leads to less pressure drop across the filter. The new setup offered easier access to the filter due to it being mounted outside the
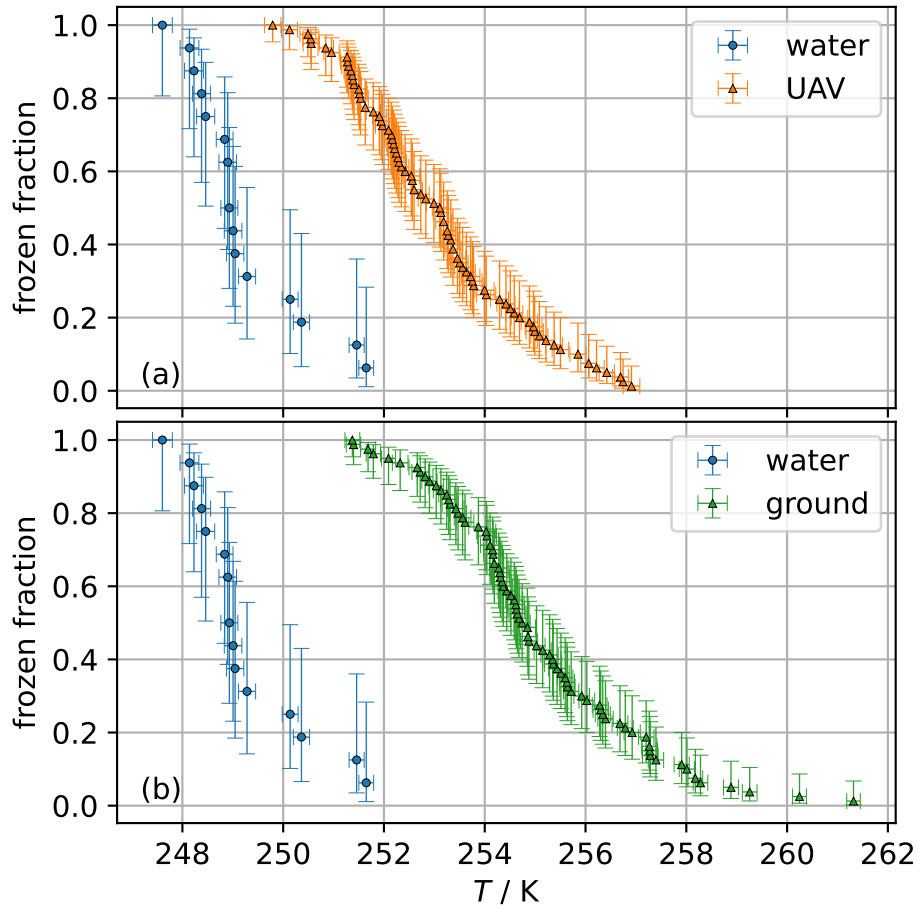
Figure 6. The frozen fraction as a function of the freezing temperature T is shown for a UAV filter suspension from campaign 1 in comparison to its Nanopure water background (panel (a)). Panel (b) shows the equivalent for the ground filters. The errorbars represent the 95 % confidence interval.

fuselage. As a result of this increase in pressure downstream of the filter, the micro-diaphragm pump maintains an increased flow rate. The flight time was shorter (from about 90 minutes down to 60 minutes), due to additional weight, but this was partly compensated for by the increase in flow (from about $10.3\,\mathrm{l\,min^{-1}}$ to $11.1\,\mathrm{l\,min^{-1}}$ at $500\,\mathrm{m}$ asl) and the decrease in transport losses. The INP detection limit can further be decreased by flying the same filter multiple times, therefore increasing the volume of sampled air. By this, the onset of freezing can be observed towards higher temperatures. Even though only three flights were conducted, the setup shown in figure 1 was tested successfully with a higher flow and easier handling in the field.
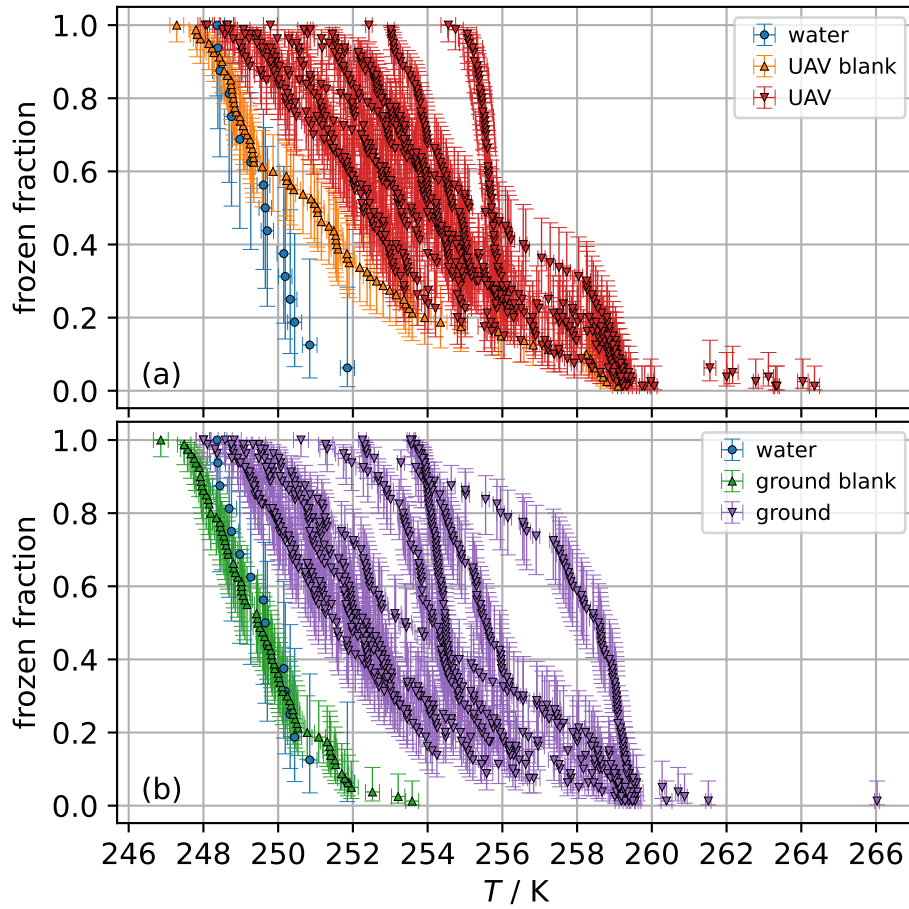
Figure 7. The frozen fraction as a function of the freezing temperature T is shown for the UAV filter suspensions from campaign 2 in comparison to its blank filter suspension and the Nanopure water background (panel (a)). Panel (b) shows the equivalent for the ground filters. The blanks were handled the same way as the filter, but the pump was not turned on, and the UAV was not flying (see Sect. 2.4). The errorbars represent the 95 % confidence interval.

4 Conclusions and Outlook

A lightweight and mobile unit was developed for sampling atmospheric aerosols either on a fixed-wing UAV or on the ground. The filter-based setup was used and further improved during three field campaigns to collect INPs in low aerosol concentration environments (i.e., northern Finland, Lohila et al., 2015) at different heights up to 1 km agl. The sampling flow was continuously measured to ensure a constant flow over the sampling period, whereas the actual flow was calculated with the average pressure during the sampling period. Ambient sensors for temperature, T, relative humidity, RH, and pressure, p, give additional information regarding current conditions and, in the case of the pressure measurement, the mass flow as well as the height of the flight, alongside GNSS data.
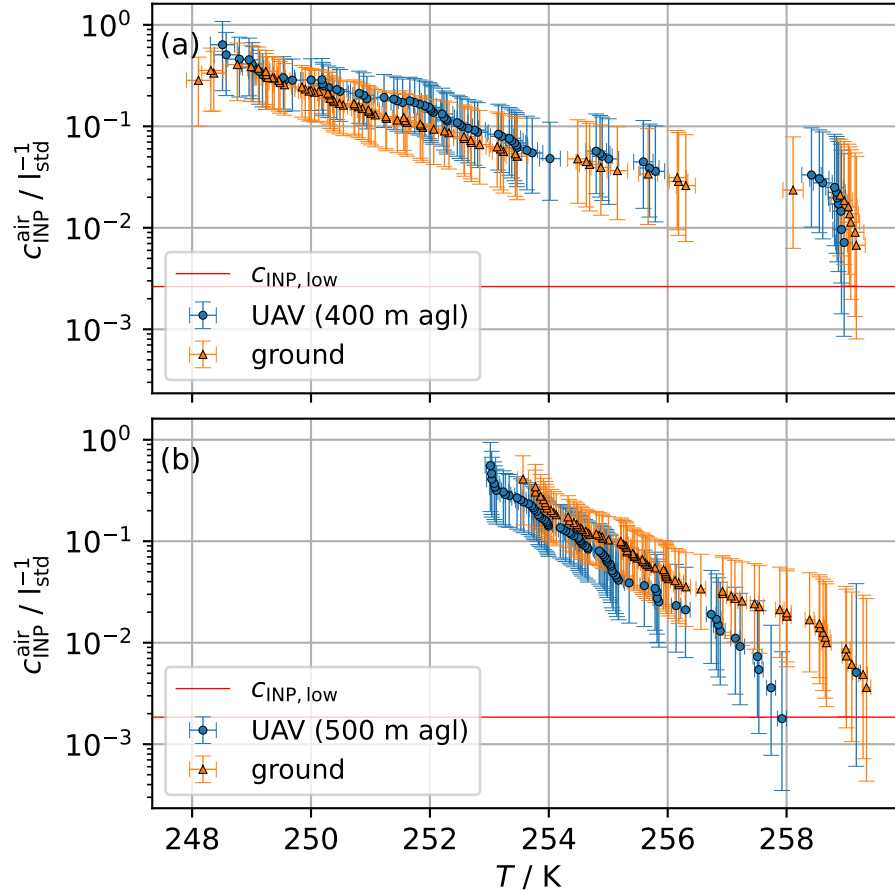
Figure 8. Panel (a) shows the INP concentration in air, $c_{\mathrm{INP}}^{\mathrm{air}}$, at 400 m agl as a function of the freezing temperature, T, for a UAV and a ground (GR) filter during campaign 2. Both filters agree very well with each other. On panel (b), the same is shown for two filters one day after at 500 m agl. This filter was flown two times, doubling its sampling time and therefore increasing the amount of air sampled (note also the decreased lower detection limit as a red horizontal line, Eq. (3)). It can be seen that lower INP concentrations can be detected due to the increased sampling time. The freezing curve does not reach the water background on panel (b). This is due to the fact that no dilution was prepared, and therefore the water background was not reached with the higher amount of INPs that can freeze a well. The errorbars represent the 95 % confidence interval.

The development of the setup is described in detail in this study, where the final system was optimised for field measurements in locations with low aerosol loadings. This is especially important in clean-air environments such as the Arctic (Bigg, 1996; Hatakka et al., 2003; Lohila et al., 2015; Šantl Temkiv et al., 2019). In addition, options for different operations, i.e. flying one filter multiple times to reach a lower detection limit, were tested (see Fig. 8, panel (b)). Typical detection limits for the setup for one flight are around $c_{\mathrm{INP,low}}^{*} = 1 \cdot 10^{-3} \, \mathrm{l_{std}}^{-1}$. This detection limit can be decreased by sampling the same filter on multiple flights. Some flights show a difference between the UAV filter compared to a concurrent ground-based filter, but based

on the current dataset it is not possible to draw a statistically relevant conclusion. This setup is able to measure the vertical
distribution of INPs in a cheap and flexible way compared to aircraft or balloon-borne setups. The current work provides a
solid foundation for understanding INP concentrations in varied atmospheric conditions. Additional measurements will further
enhance the statistical robustness and reliability of our findings.

Future experiments will include aerosol particle size distribution measurements in addition to INP measurements via small,
lightweight optical particle counters. The Universal Cloud and Aerosol Sounding System (UCASS) would open up this pos-
sibility (Smith et al., 2019; Girdwood et al., 2020). More measurements, for longer operation periods, in conjunction with
other similar measurement platforms, i.e. ballon-borne, and at different heights, are planned and will increase knowledge about
height-resolved INP concentrations inside the planetary boundary layer. These measurement periods will allow the additional
use of backwards trajectories to estimate the sources of aerosols at different altitudes. A vertical distribution of INP concen-
trations could also be helpful to validate as well as complement models to connect ground- and aircraft-based measurements.
This is the case especially in the Arctic due to its characteristically stratified atmosphere (Graversen et al., 2008).

Code and data availability. The code for the calculation of the transport efficiency is available at https://codebase.helmholtz.cloud/alexander.
boehmlaender/as_tools. The code for the creation of the plots and analysis of raw data is available from the author upon request. Data sets
are available at https://radar.kit.edu/radar/en/dataset/ecljSTKjCuIoqEkr?token=sSJKlzwZKHYlpepdBzaK.

Appendix A: Uncertainty budget of INSEKT

The uncertainties of the preparation of the solutions as well as the washing water need to be considered during analysis. The
uncertainties are calculated via propagation of uncertainty from the formula

$$c_{INP,air} = \frac{V_{sol}}{V_{air}} \frac{d}{V_{well}} \ln\left(\frac{f_{1,np}}{f_1}\right) . \tag{A1}$$

This results in the following formula for the variance:

$$\text{Var}(c_{INP,air}) = c_{INP,air}^2 \left[\left(\frac{\Delta V_{sol}}{V_{sol}}\right)^2 + \left(\frac{\Delta V_{well}}{V_{well}}\right)^2 + \left(\frac{\Delta V_{air}}{V_{air}}\right)^2 + \left(\frac{\Delta d_n}{d_n}\right)^2\right] , \tag{A2}$$

where d_n denotes a specific dilution (see Eq. (A7)).

The uncertainty of the solution volume is dependent on its preparation and can therefore vary for different experiments. In
general, it is given by the weighted sum of the pipette uncertainties

$$\frac{\Delta V_{sol}}{V_{sol}} = \frac{\sum_i w_i V_i}{V_{sol}} , \tag{A3}$$

where the weights w_i are given by the fraction of pipette and solution volume. The uncertainty of the well volume is given by
the electrical pipette (Eppendorf Xplorer® plus, Eppendorf, see Table A1) that is used to fill each well

$$\frac{\Delta V_{well}}{V_{well}} = \frac{6\% \cdot 50\,\mu l + 1\% \cdot 50\,\mu l}{50\,\mu l} = 7\% . \tag{A4}$$

The volume of air sampled is calculated with the measured mass flow and the duration of the sampling, therefore the corresponding uncertainty is given as

$$\frac{\Delta V_{\mathrm{air}}}{V_{\mathrm{air}}} = \sqrt{\left(\frac{\Delta F_{\mathrm{std}}}{F_{\mathrm{std}}}\right)^2 + \left(\frac{\Delta t}{t}\right)^2} ,\qquad\qquad (A5)$$

255 where the uncertainty of the time measurement is just given by the least count, i.e. half a minute. The uncertainty of the flow can be estimated via propagation of uncertainty from the fitting function (see app. C) as

$$\Delta F_{\mathrm{std}} = \sqrt{(p\Delta m_i)^2 + (m_i\Delta p)^2 + (\Delta c_i)^2}\qquad\qquad (A6)$$

with i denoting the different fitting parameters and p the pressure measured with the BME280 sensor.

The uncertainty of the dilution scale is given by

$$d_n = \left(\frac{V_0 + V_d}{V_d}\right)^n ,$$

260
$$\frac{\Delta d_n}{d_n} = n\left(\frac{V_d}{V_0 + V_d}\right)\sqrt{\left(\frac{\Delta V_0}{V_0}\right)^2 + \left(\frac{V_0}{V_d}\right)^2\left(\frac{\Delta V_d}{V_d}\right)^2}\qquad\qquad (A7)$$

with n denoting the dilution step (i.e. 0, 1, 2, ...), V_0 the volume of the Nanopure water in the dilution, and V_d the volume of the washing water in the dilution. These systematic uncertainties are usually up to two orders of magnitude smaller than the statistical uncertainties; therefore, they are omitted from the plots for simplicity.

Appendix B: Transport efficiency

265 The theoretical calculations of the transport efficiency are dependent on a multitude of factors, one of them the flow regime. The Reynolds number, Re, is given as

$$\mathrm{Re} = \frac{v_{\mathrm{m}} d}{\nu} \approx 4100 ,\qquad\qquad (B1)$$

where the mean velocity, v_{m}, is calculated with a flow of $10\,\mathrm{l\,min^{-1}}$ and a tube diameter, $d = 4\cdot10^{-3}\,\mathrm{m}$. The value for the kinematic viscosity of air at $T = 273.15\,\mathrm{K}$ is calculated from the viscosity as described in Kulkarni (2011) (Eq. (2-8) and Table
270 2.1 therein).

Table A1. Uncertainties of the INSEKT pipettes (Eppendorf, 2021a, b).

Device	Value	Systematic uncertainty		Random uncertainty	
		$\pm\%$	$\pm\Delta$	$\pm\%$	$\pm\Delta$
Eppendorf Research® plus,	5 ml	0.6	30 µl	0.15	8 µl
violet	2.5 ml	1.2	30 µl	0.25	6 µl
Eppendorf Research® plus, blue	100 µl	3	3 µl	0.6	0.6 µl
Eppendorf Xplorer® plus, blue	50 µl	6	3 µl	1	0.5 µl
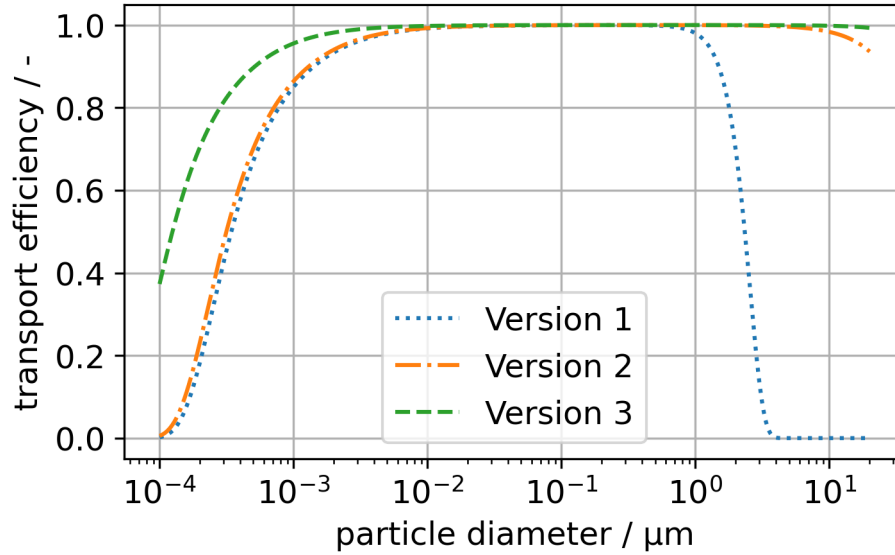
Figure B1. The total transport efficiency is calculated for all three setups used in the three campaigns. Especially larger particles have a larger transport efficiency due to the removal of bends for the second setup and the increase in flow for the third setup. The decrease in the flow path length benefits the collection of small particles due to the decreased diffusional losses.

The resulting transport efficiency considers diffusional losses from small particles ($d_\mathrm{p} \leq 20\,\mathrm{nm}$) and losses of larger particles via sedimentation, inertial effects, and turbulent deposition (Kulkarni, 2011; Wendisch et al., 2004). The resulting efficiency as a function of particle diameter in the respective flow regime is shown in Fig. B1. The parameters are detailed in Table B1.

Table B1. Parameters for the calculation of the transport efficiency in all three setups.

Parameter	1$^\mathrm{st}$ setup	2$^\mathrm{nd}$ setup	3$^\mathrm{rd}$ setup
Tube length / m	$172 \cdot 10^{-3}$	$145 \cdot 10^{-3}$	$20 \cdot 10^{-3}$
Tube diameter / m		$6 \cdot 10^{-3}$	$4 \cdot 10^{-3}$
Flow / $l\,\mathrm{min}^{-1}$		10	11
Ambient pressure / Pa		95000	
Ambient temperature / K		273.15	
Inclination angle / °		0	
Bend angle / °	90		—
Number of bends / —	2		0
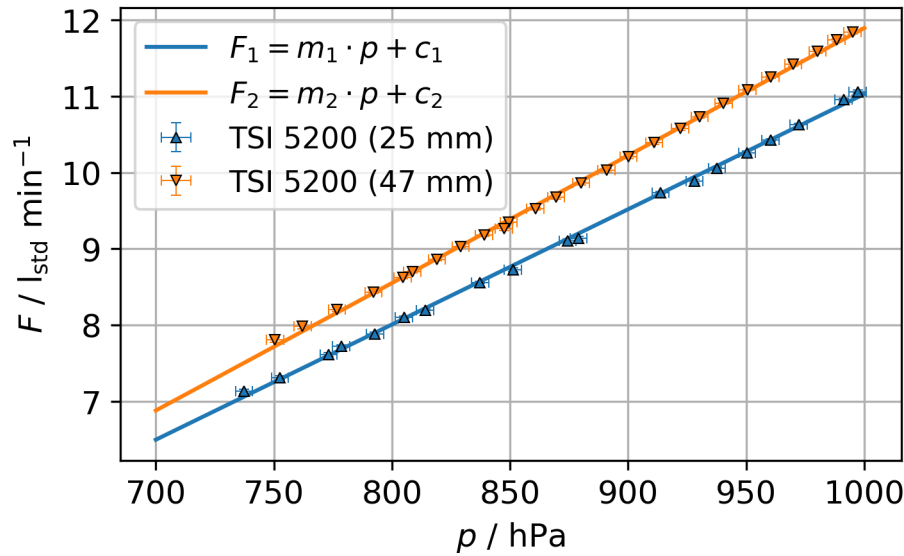
Figure C1. The flow was measured with a flow meter (TSI 5200, TSI) and created by the micro-diaphragm pump at different pressures. The pressure was measured by a pressure sensor (VD85, Thyracont) in line with the flow upstream of the filter. The uncertainty of the flow is obtained from the standard deviation of the mean during measurement. The uncertainty on the pressure is taken from the data sheet of the respective sensors (VD85, 0.3 % of full scale, Thy).

Appendix C: Flow calculation

275   The micro-diaphragm pump consists of two diaphragms that are shifted by about 180° and therefore produce a flow that follows an absolute sinus curve. The maximal values of this sinus are higher than the rated full scale of the flow meter (SFM4100). Therefore, the flow meter used in the setup will always underestimate the flow. The flow meter is still useful since one can determine if there was any flow over the filter or if there was any change during filter sampling, which can occur on a UAV due to vibrations, for instance. The pump was tested in the lab in combination with a needle valve, a pressure sensor (VD85,

280   Thyracont), and a flow meter (TSI 5200, TSI) to measure the mass flow at different pressures. Figure C1 shows the linear nature of the dependence of the flow on the pressure in the observed pressure range. Using the pressure from the VD85 sensor, orthogonal distance regression (ODR, Boggs and Rogers (1990)) was used to estimate the flow during a flight in dependence of the pressure.

Author contributions.   AB wrote this manuscript and performed the data and filter analysis. LL and OM provided scientific discussion as well

285   as proofreading of the whole manuscript. DB and KD contributed to the manuscript and were responsible for flying the fixed-wing during all campaigns. ZB and MB took care of flying and filter changing during the spring 2021 campaign. JK was responsible for the design and printing of the 3D pieces. TL has written the LabVIEW code for INSEKT and assisted during data extraction.

Competing interests. The authors declare that they have no conflict of interest.

Acknowledgements. Map data copyrighted OpenStreetMap contributors and available from https://www.openstreetmap.org. We gratefully
290 acknowledge support from the technical and engineering team members at IMK-AAF, in particular Jens Nadolny. This work received financial
support through the Helmholtz program "The Atmosphere in Global Change", and was part of a transnational access project that was
supported by the European Commission under the Horizon 2020 – Research and Innovation Framework Programme, H2020-INFRAIA-
2020-1, ATMO-ACCESS Grant Agreement number: 101008004. Zoé Brasseur and Matthew Boyer acknowledge support from the European
Research Council (ERC) grant no. 714621.

295 References

VD85, Thyracont Vacuum Instruments GmbH, vd85-220101 edn.

Agresti, A. and Coull, B. A.: Approximate is Better than "Exact" for Interval Estimation of Binomial Proportions, The American Statistician, 52, 119–126, https://doi.org/10.1080/00031305.1998.10480550, 1998.

Barry, K. R., Hill, T. C. J., Jentzsch, C., Moffett, B. F., Stratmann, F., and DeMott, P. J.: Pragmatic protocols for working cleanly when
300   measuring ice nucleating particles, Atmospheric Research, 250, 105 419, https://doi.org/10.1016/j.atmosres.2020.105419, 2021.

Bergeron, T.: Proces Verbaux de l'Association de Météorologie, in: International Union of Geodesy and Geophysics, pp. 156–178, 1935.

Bieber, P., Seifried, T. M., Burkart, J., Gratzl, J., Kasper-Giebl, A., Schmale, D. G., and Grothe, H.: A Drone-Based Bioaerosol Sampling System to Monitor Ice Nucleation Particles in the Lower Atmosphere, Remote Sensing, 12, 552, https://doi.org/10.3390/rs12030552, 2020.

305 Bigg, E. K.: Ice forming nuclei in the high Arctic, Tellus Ser. B, 48, 223–233, https://doi.org/10.3402/tellusb.v48i2.15888, 1996.

Boggs, P. T. and Rogers, J. E.: Orthogonal Distance Regression, in: Statistical analysis of measurement error models and applications: proceedings of the AMS-IMS-SIAM joint summer research conference held June 10-16, 1989, vol. 112 of *Contemporary Mathematics*, p. 186, 1990.

Bosch: BME280 - Data sheet, Bosch Sensortec, 1.9 edn., BME280 sensor specifications, 2020.

310 Boucher, O., Randall, D., Artaxo, P., Bretherton, C., Feingold, G., Forster, P., Kerminen, V.-M., Kondo, Y., Liao, H., Lohmann, U., Rasch, P., Satheesh, S. K., Sherwood, S., Stevens, B., and Zhang, X. Y.: Clouds and Aerosols, book section 7, pp. 571–658, Cambridge University Press, Cambridge, United Kingdom and New York, NY, USA, ISBN 978-1-107-66182-0, https://doi.org/10.1017/CBO9781107415324.016, 2013.

Bärfuss, K., Pätzold, F., Altstädter, B., Kathe, E., Nowak, S., Bretschneider, L., Bestmann, U., and Lampert, A.: New Setup
315   of the UAS ALADINA for Measuring Boundary Layer Properties, Atmospheric Particles and Solar Radiation, Atmosphere, 9, https://doi.org/10.3390/atmos9010028, 2018.

Creamean, J., Hill, T., Hume, C., and Devadoss, T.: Ice Nucleation Spectrometer (INS) Instrument Handbook, techreport, U.S. Department of Energy, Atmospheric Radiation Measurement user facility, Richland, Washington, dOE/SC-ARM-TR-278, 2024.

Creamean, J. M., Primm, K. M., Tolbert, M. A., Hall, E. G., Wendell, J., Jordan, A., Sheridan, P. J., Smith, J., and Schnell, R. C.: HOV-
320   ERCAT: a novel aerial system for evaluation of aerosol–cloud interactions, Atmospheric Measurement Techniques, 11, 3969–3985, https://doi.org/10.5194/amt-11-3969-2018, 2018.

DeMott, P. J., Prenni, A. J., Liu, X., Kreidenweis, S. M., Petters, M. D., Twohy, C. H., Richardson, M. S., Eidhammer, T., and Rogers, D. C.: Predicting global atmospheric ice nuclei distributions and their impacts on climate, Proceedings of the National Academy of Sciences, 107, 11 217–11 222, https://doi.org/10.1073/pnas.0910818107, 2010.

325 DeMott, P. J., Hill, T. C. J., Petters, M. D., Bertram, A. K., Tobo, Y., Mason, R. H., Suski, K. J., McCluskey, C. S., Levin, E. J. T., Schill, G. P., Boose, Y., Rauker, A. M., Miller, A. J., Zaragoza, J., Rocci, K., Rothfuss, N. E., Taylor, H. P., Hader, J. D., Chou, C., Huffman, J. A., Pöschl, U., Prenni, A. J., and Kreidenweis, S. M.: Comparative measurements of ambient atmospheric concentrations of ice nucleating particles using multiple immersion freezing methods and a continuous flow diffusion chamber, Atmos. Chem. Phys., 17, 11 227–11 245, https://doi.org/10.5194/acp-17-11227-2017, 2017.

330 Desai, N., Chandrakar, K. K., Kinney, G., Cantrell, W., and Shaw, R. A.: Aerosol-Mediated Glaciation of Mixed-Phase Clouds: Steady-State Laboratory Measurements, Geophysical Research Letters, 46, 9154–9162, https://doi.org/10.1029/2019gl083503, 2019.

Eppendorf: Eppendorf Xplorer® plus – Technical Data, 2021a.

Eppendorf: Eppendorf Researcher® plus – Technical Data, 2021b.

Field, P. R. and Heymsfield, A. J.: Importance of snow to global precipitation, Geophysical Research Letters, 42, 9512–9520, https://doi.org/10.1002/2015gl065497, 2015.

Findeisen, W.: Die kolloidmeteorologischen Vorgänge bei der Niederschlagsbildung (Colloidal meteorological processes in the formation of precipitation; translated and edited by Volken, E., Giesche, A. M. and Brönnimann. S., Meteorol. Z., 24, 443 – 454, 2015), Meteorol. Z., 55, 121–133, https://doi.org/10.1127/metz/2015/0675, 1938.

Girdwood, J., Smith, H., Stanley, W., Ulanowski, Z., Stopford, C., Chemel, C., Doulgeris, K.-M., Brus, D., Campbell, D., and Mackenzie, R.: Design and field campaign validation of a multi-rotor unmanned aerial vehicle and optical particle counter, Atmospheric Measurement Techniques, 13, 6613–6630, https://doi.org/10.5194/amt-13-6613-2020, 2020.

Graversen, R. G., Mauritsen, T., Tjernström, M., Källén, E., and Svensson, G.: Vertical structure of recent Arctic warming, Nature, 451, 53–56, https://doi.org/10.1038/nature06502, 2008.

Hatakka, J., Aalto, T., Aaltonen, V., Aurela, M., Hakola, H., Komppula, M., Laurila, T., Lihavainen, H., Paatero, J., Salminen, K., and Viisanen, Y.: Overview of the atmospheric research activities and results at Pallas GAW station, Boreal Environment Research, 8, 2003.

He, C., Yin, Y., Wang, W., Chen, K., Mai, R., Jiang, H., Zhang, X., and Fang, C.: Aircraft observations of ice nucleating particles over the Northern China Plain: Two cases studies, Atmospheric Research, 248, 105 242, https://doi.org/10.1016/j.atmosres.2020.105242, 2021.

Heymsfield, A. J., Schmitt, C., Chen, C.-C.-J., Bansemer, A., Gettelman, A., Field, P. R., and Liu, C.: Contributions of the Liquid and Ice Phases to Global Surface Precipitation: Observations and Global Climate Modeling, Journal of the Atmospheric Sciences, 77, 2629–2648, https://doi.org/10.1175/jas-d-19-0352.1, 2020.

Hill, T. C. J., DeMott, P. J., Tobo, Y., Fröhlich-Nowoisky, J., Moffett, B. F., Franc, G. D., and Kreidenweis, S. M.: Sources of organic ice nucleating particles in soils, Atmospheric Chemistry and Physics, 16, 7195–7211, https://doi.org/10.5194/acp-16-7195-2016, 2016.

Hoose, C. and Möhler, O.: Heterogeneous ice nucleation on atmospheric aerosols: a review of results from laboratory experiments, Atmos. Chem. Phys., 12, 9817–9854, https://doi.org/10.5194/acp-12-9817-2012, 2012.

IPCC: Climate Change 2021: The Physical Science Basis. Contribution of Working Group 1 to the Sixth Assessment Report of the Intergovernmental Panel on Climate Change, Cambrige University Press, in Press, 2021.

Kanji, Z. A., Ladino, L. A., Wex, H., Boose, Y., Burkert-Kohn, M., Cziczo, D. J., and Krämer, M.: Overview of Ice Nucleating Particles, Meteorological Monographs, 58, 11–133, https://doi.org/10.1175/amsmonographs-d-16-0006.1, 2017.

KNF: Micro Membran Gasförderpumpen, KNF, BA321648-321650.

Korolev, A., McFarquhar, G., Field, P. R., Franklin, C., Lawson, P., Wang, Z., Williams, E., Abel, S. J., Axisa, D., Borrmann, S., Crosier, J., Fugal, J., Krämer, M., Lohmann, U., Schlenczek, O., Schnaiter, M., and Wendisch, M.: Mixed-Phase Clouds: Progress and Challenges, Meteorol. Monogr., 58, 51–550, https://doi.org/10.1175/amsmonographs-d-17-0001.1, 2017.

Kulkarni, P.: Aerosol measurement : principles, techniques, and applications, Wiley, Hoboken, N.J, ISBN 9780470387412, 2011.

Lampert, A., Altstädter, B., Bärfuss, K., Bretschneider, L., Sandgaard, J., Michaelis, J., Lobitz, L., Asmussen, M., Damm, E., Käthner, R., Krüger, T., Lüpkes, C., Nowak, S., Peuker, A., Rausch, T., Reiser, F., Scholtz, A., Sotomayor Zakharov, D., Gaus, D., Bansmer, S., Wehner, B., and Pätzold, F.: Unmanned Aerial Systems for Investigating the Polar Atmospheric Boundary Layer—Technical Challenges and Examples of Applications, Atmosphere, 11, https://doi.org/10.3390/atmos11040416, 2020.

Lohila, A., Penttilä, T., Jortikka, S., Aalto, T., Anttila, P., Asmi, E., Aurela, M., Hatakka, J., Hellén, H., Henttonen, H., Hänninen, P., Kilkki, J., Kyllönen, K., Laurila, T., Lepistö, A., Lihavainen, H., Makkonen, U., Paatero, J., Rask, M., Sutinen, R., Tuovinen, J.-P., Vuorenmaa,

370   J., and Viisanen, Y.: Preface to the special issue on integrated research of atmosphere, ecosystems and environment at Pallas, in: Boreal Environment Research, vol. 20, pp. 431–454, 2015.

Lohmann, U.: Anthropogenic Aerosol Influences on Mixed-Phase Clouds, Current Climate Change Reports, 3, 32–44, https://doi.org/10.1007/s40641-017-0059-9, 2017.

Marinou, E., Tesche, M., Nenes, A., Ansmann, A., Schrod, J., Mamali, D., Tsekeri, A., Pikridas, M., Baars, H., Engelmann, R., Voudouri,

375   K. A., Solomos, S., Sciare, J., Groß, S., Ewald, F., and Amiridis, V.: Retrieval of ice-nucleating particle concentrations from lidar observations and comparison with UAV in situ measurements, Atmos. Chem. Phys., 19, 11 315–11 342, https://doi.org/10.5194/acp-19-11315-2019, 2019.

Murray, B. J., O'Sullivan, D., Atkinson, J. D., and Webb, M. E.: Ice nucleation by particles immersed in supercooled cloud droplets, Chemical Society Reviews, 41, 6519, https://doi.org/10.1039/c2cs35200a, 2012.

380   Murray, B. J., Carslaw, K. S., and Field, P. R.: Opinion: Cloud-phase climate feedback and the importance of ice-nucleating particles, Atmospheric Chemistry and Physics, 21, 665–679, https://doi.org/10.5194/acp-21-665-2021, 2021.

Mülmenstädt, J., Sourdeval, O., Delanoë, J., and Quaas, J.: Frequency of occurrence of rain from liquid-, mixed-, and ice-phase clouds derived from A-Train satellite retrievals, Geophys. Res. Lett., 42, 6502–6509, https://doi.org/10.1002/2015GL064604, 2015.

Porter, G. C. E., Sikora, S. N. F., Adams, M. P., Proske, U., Harrison, A. D., Tarn, M. D., Brooks, I. M., and Murray, B. J.: Resolving

385   the size of ice-nucleating particles with a balloon deployable aerosol sampler: the SHARK, Atmospheric Measurement Techniques, 13, 2905–2921, https://doi.org/10.5194/amt-13-2905-2020, 2020.

Pruppacher, H. R. and Klett, J. D.: Microphysics of Clouds and Precipitation, Kluwer Acad. Norwell, Mass, 1997.

Schneider, J., Höhler, K., Heikkilä, P., Keskinen, J., Bertozzi, B., Bogert, P., Schorr, T., Umo, N. S., Vogel, F., Brasseur, Z., Wu, Y., Hakala, S., Duplissy, J., Moisseev, D., Kulmala, M., Adams, M. P., Murray, B. J., Korhonen, K., Hao, L., Thomson, E. S., Castarède, D., Leisner,

390   T., Petäjä, T., and Möhler, O.: The seasonal cycle of ice-nucleating particles linked to the abundance of biogenic aerosol in boreal forests, Atmospheric Chemistry and Physics, 21, 3899–3918, https://doi.org/10.5194/acp-21-3899-2021, 2021.

Schrod, J., Weber, D., Drücke, J., Keleshis, C., Pikridas, M., Ebert, M., Cvetkovic, B., Nickovic, S., Marinou, E., Baars, H., Ansmann, A., Vrekoussis, M., Mihalopoulos, N., Sciare, J., Curtius, J., and Bingemer, H. G.: Ice nucleating particles over the Eastern Mediterranean measured by unmanned aircraft systems, Atmos. Chem. Phys., 17, 4817–4835, https://doi.org/10.5194/acp-17-4817-2017, 2017.

395   Sensirion: SFM4100 Series, Sensirion, 1.3 edn., 2013.

Sensirion: SHT4x, Sensirion, 2 edn., 2021.

Shi, Y. and Liu, X.: Dust Radiative Effects on Climate by Glaciating Mixed-Phase Clouds, Geophysical Research Letters, 46, 6128–6137, https://doi.org/10.1029/2019gl082504, 2019.

Smith, H. R., Ulanowski, Z., Kaye, P. H., Hirst, E., Stanley, W., Kaye, R., Wieser, A., Stopford, C., Kezoudi, M., Girdwood, J., Greenaway,

400   R., and Mackenzie, R.: The Universal Cloud and Aerosol Sounding System (UCASS): a low-cost miniature optical particle counter for use in dropsonde or balloon-borne sounding systems, Atmospheric Measurement Techniques, 12, 6579–6599, https://doi.org/10.5194/amt-12-6579-2019, 2019.

Storelvmo, T.: Aerosol Effects on Climate via Mixed-Phase and Ice Clouds, Annual Review of Earth and Planetary Sciences, 45, 199–222, https://doi.org/10.1146/annurev-earth-060115-012240, 2017.

405   Vali, G.: Quantitative Evaluation of Experimental Results an the Heterogeneous Freezing Nucleation of Supercooled Liquids, J. Atmos. Sci., 28, 402–409, https://doi.org/10.1175/1520-0469(1971)028<0402:qeoera>2.0.co;2, 1971.

Vali, G.: - Ice Nucleation — a review, in: Nucleation and Atmospheric Aerosols 1996, edited by Kulmala, M. and Wagner, P. E., pp. 271–279, Pergamon, Amsterdam, ISBN 978-0-08-042030-1, https://doi.org/10.1016/B978-008042030-1/50066-4, 1996.

Villa, T., Gonzalez, F., Miljievic, B., Ristovski, Z., and Morawska, L.: An Overview of Small Unmanned Aerial Vehicles for Air Quality Measurements: Present Applications and Future Prospectives, Sensors, 16, 1072, https://doi.org/10.3390/s16071072, 2016.

Wegener, A.: Thermodynamik der Atmosphäre, Verlag von Johann Ambrosius Barth, 1911.

Wendisch, M., Coe, H., Baumgardner, D., Brenguier, J.-L., Dreiling, V., Fiebig, M., Formenti, P., Hermann, M., Krämer, M., Levin, Z., Maser, R., Mathieu, E., Nacass, P., Noone, K., Osborne, S., Schneider, J., Schütz, L., Schwarzenböck, A., Stratmann, F., and Wilson, J. C.: State-of-the-Art and Future Needs, in: Aircraft Particle Inlets, 2004.

Yu, F., Liu, Y., Fan, L., Li, L., Han, Y., and Chen, G.: Design and implementation of atmospheric multi-parameter sensor for UAV-based aerosol distribution detection, Sensor Review, 37, 196–210, https://doi.org/10.1108/sr-09-2016-0199, 2017.

Šantl Temkiv, T., Lange, R., Beddows, D., Rauter, U., Pilgaard, S., Dall'Osto, M., Gunde-Cimerman, N., Massling, A., and Wex, H.: Biogenic Sources of Ice Nucleating Particles at the High Arctic Site Villum Research Station, Environmental Science & Technology, 53, 10 580–10 590, https://doi.org/10.1021/acs.est.9b00991, 2019.